Environ Sci Pollut Res (2016) 23:6546–6562
DOI 10.1007/s11356-015-5860-1

RESEARCH ARTICLE

Aerosol composition and properties variation at the ground and over the column under different air masses advection in South Italy

G. Pavese[1] · A. Lettino[1] · M. Calvello[1] · F. Esposito[2] · S. Fiore[1]

Received: 30 June 2015 / Accepted: 23 November 2015 / Published online: 4 December 2015

Abstract Aerosol composition and properties variation under the advection of different air masses were investigated, as case studies, by contemporary measurements over the atmospheric column and at the ground in a semi-rural site in South Italy. The absence of local strong sources in this area allowed to characterize background aerosol and to compare particle mixing effects under various atmospheric circulation conditions. Aerosol optical depth (AOD) and Ångström parameters from radiometric measurements allowed the detection and identification of polluted, dust, and volcanic atmospheric conditions. AODs were the input for a suitable model to evaluate the columnar aerosol composition, according to six main tmospheric components (water-soluble, soot, sea salt accumulation, sea salt coarse, mineral dus,t and biological). Scanning electron microscope (SEM) analysis of particulate sampled with a 13-stage impactor at the ground showed not only fingerprints typical of the different air masses but also the effects of transport and aging on atmospheric particles, suggesting processes that changed their chemical and optical properties. Background columnar aerosol was characterized by 72 % of water-soluble and soot, in agreement with ground-based findings that highlighted 60 % of contribution from anthropogenic carbonate particles and soot. In general, a good agreement between ground-based and columnar results was observed. Under the advection of trans-boundary air masses, water-soluble and soot were always present in columnar aerosol, whereas, in variable percentages, sea salt and mineral particles characterized both dust and volcanic conditions. At the ground, sulfates characterized the amorphous matrix produced in finer stages by the evaporation of solutions of organic and inorganic aerosols. Sulfates were also one of the key players involved in heterogeneous chemical reactions, producing complex secondary aerosol, as such clay-sulfate internally mixed particle externally mixed with soot chains.

Keywords Atmospheric aerosol · Radiometric measurements · Gravimetric measurements · SEM-EDX analysis · Trans-boundary aerosol · Aerosol mixing effects

Responsible editor: Constantini Samara

✉ G. Pavese
giulia.pavese@imaa.cnr.it

[1] Consiglio Nazionale delle Ricerche-Istituto di Metodologie per l'Analisi Ambientale (CNR-IMAA), C.da S. Loja, 85050, Tito Scalo Potenza, Italy

[2] Università della Basilicata-Scuola di Ingegneria, C.da Macchia Romana, 85100 Potenza, Italy

Introduction

Atmospheric aerosols are one of the major components that impact atmospheric processes, influencing both global radiative budget and cloud formation and causing climate variations (IPCC 2007). Furthermore, research findings have shown direct effects on human health related to their inhalability. These negative effects (cardiovascular and respiratory disorders) can be reinforced due to their diverse sources and chemical composition, also in presence of short-term exposure to PM2.5, as studied in the "Denver Aerosol Sources and Health (DASH) study" (Vedal et al. 2009).

Anthropogenic activities heavily contribute to aerosol production, such as in emerging nations (China and India) or in Eastern Europe, and is considered an important source of anthropogenic particles due to the presence of both obsolete plants in heavy industry and open mines, as well as intensive agricultural activities (Bovchaliuk et al. 2013).

Atmospheric circulation of air masses spreads anthropogenic and natural particles (i.e., pollen and Saharan and/or Asian dust) around the world. Experimental evidence of aerosol transport, such as the transpacific transport of dust and pollutants from Asia to North America, anthropogenic contribution of European and Asian emissions and wild fires to the Arctic, long-range transport of biomass burning, and Saharan dust over the Mediterranean Sea and Southern Europe, can be found in literature (Papayannis et al. 2005; Sciare et al. 2008; Eguchi et al. 2009; de Villiers et al. 2010; Pederzoli et al. 2010; Pavese et al. 2012; Lettino et al. 2012).

Moreover, air masses circulation favor aerosol mixing states (Bauer et al. 2013) and dramatic radiative properties variations: recently, the importance to include mixing mechanism of soot in radiative forcing models have been highlighted (Cheng et al. 2015).

Multi-instrument measurements campaigns, focused on specific topics (Pavese et al. 2009). are able to gather and improve information on aerosol properties and atmospheric processes, particularly those trying to find a relationship, if any, between ground-based and columnar data. In a latest study (Perrone et al. 2015). columnar and ground-based parameters as such, respectively, aerosol optical depth (AOD), Ångström exponent, asymmetry parameter and scattering coefficient, scattering Ångström exponent, asymmetry parameter have been compared to infer the impact of local and transboundary pollution in Central Mediterranean.

From the analysis of 1 year of data from Hyderabad (India) (Sinha et al. 2013). similar time behaviors of AOD measured in the atmospheric boundary layer and of black carbon (BC) content at ground level were found, suggesting carbonaceous particles as one of the major contributors to the aerosol content in the boundary layer. Similarly, the comparison of fine fractions from both gravimetric mass distributions and columnar radiometric size distributions and BC content in PM2.5 in a semirural site in South Italy (Calvello et al. 2010) results in a good agreement under northeast European polluted air masses, highlighting the predominance of surface aerosol optical properties over the entire atmospheric column.

Radiometric measurements can be used also as an input to derive columnar aerosol composition when aerosol parameters are coupled with a suitable model allowing the identification of the main atmospheric particulate components. For example, considering data from a short measurement campaign (1–14 May) in Cabauw (the Netherlands) (van Beelen et al. 2014). an atmospheric aerosols composition as a combination of sulfates, ammonium nitrate, organic matter, and black carbon particles was suggested. Instead, a chemical characterization of aerosol properties, on monthly and seasonal bases, derived by radiometric measurements from a mining site located in a Monsoon Trough Region (Latha et al. 2014) was obtained by the Optical Properties of Aerosols and Clouds (OPAC) model (Hess et al. 1998). Due to the site characteristics, the main components were water-soluble, insoluble, soot, sea salt accumulation, mineral accumulation, and coarse and mineral dust transported above the boundary layer.

Useful information about the aerosol sources, their reactivity and transport can be inferred by scanning electron microscope (SEM) analysis of in situ particle deposits (Ebert et al. 2000, 2004; Shi et al. 2003; Li et al. 2010; Tiwari et al. 2015). Moreover, the analysis of size-selected samples is effective to improve the knowledge on processes, such as partitioning, recrystallization of secondary aerosol phases and element chemical speciation, where particle dimension plays a fundamental role.

The present study aims to study the effects of long-range transport on aerosol properties and composition, both at the ground and over the atmospheric column, by combining radiometric measurements and SEM analysis results, to improve particle characterization in a semirural site in South Italy. As the measurements location is far from regions of strong particle emissions, aerosol properties are expected to be affected by possible chemical processes occurring along great distance paths.

Instruments and methods

Direct solar irradiance measurements were obtained in the UV–vis range with a manually operated Ocean Optics S2000, over the spectral range of 400–800 nm with a 1-nm resolution and time resolution of 15 min from sunrise to sunset. The presence of an operator ensured clear sky conditions during data collection. The full procedure for radiometric measurement processing is described in Esposito et al. (2004). In particular, the well-known Langley technique is applied to calibrate irradiance spectra and to estimate the AODs outside of the strong gaseous bands, whereas an appropriate inversion technique (Amato et al. 1995) allowed the retrieval of size distributions in the radii range of 0.1 to 3 μm, where it has been verified to be more reliable.

The ground level mass size distributions were obtained by means of a 13-stage Dekati low-pressure impactor (DLPI) with an equivalent aerodynamic diameter (EAD) ranging from 0.03 to 10 μm. The instrument was equipped with 25-mm-diameter Nucleopore polycarbonate filters to perform gravimetric measurements and SEM analysis on aerosols collected during a 24-h sampling time. The mean daily values of atmospheric parameters, such as temperature, pressure, and relative humidity, were measured at the impactor inlet to estimate the normalized sampled volume. Filters were properly conditioned before and after the sampling period according to the procedure described in Calvello et al. (2010).

DLPI filters were observed by means of a field emission scanning electron microscope (FESEM, Zeiss Supra 40) equipped with an energy-dispersive X-ray spectrometer

(EDS, Oxford Inca Energy 350), allowing characterization of grains as small as some tens of nanometers with high-resolution images from an in-lens secondary electron detector. A small portion (0.5 cm^2) of the filters was attached to an aluminum stub (12 mm in diameter) using a carbon sticky tab and subsequently carbon coated: samples were studied on images by secondary electron (SE) and back-scattered electron (BSE) detectors. The energy-dispersive X-ray (EDX) analysis was performed with an energy dispersive Si(Li) detector with an ultra-thin window (INCA SATW) capable of detecting elements with an atomic number Z >4. Nevertheless, only elements with Z >10 (Na) were considered in the X-ray spectra evaluation because the samples were carbon-coated, and carbon and oxygen were present in polycarbonate filters. X-ray spectra were acquired at a 15-kV accelerating voltage using a 30-mm aperture size.

Identification of aerosol components from the columnar AOD

To evaluate the contribution of the aerosol components to the columnar AOD, a least-square technique was applied to the radiometric data set under examination (Satheesh and Srinivasan 2005).

The aerosol number size distributions $n(r)$ were considered as the sum of individual aerosol species $n_j(r)$ that are commonly used in radiative transfer models:

$$n(r) = \sum_{j=1}^{k} n_j(r) \quad (1)$$

In particular, five aerosol types used in OPAC model (Hess et al. 1998) (water-soluble (WS), soot (S), sea salt coarse mode (SScoa), sea salt accumulation mode (SSacc), and mineral dust (MD)) plus a primary biological component (Matthias-Maser and Jaenicke 1995 and Huffman et al. 2010) were considered. The corresponding physical (mean radius, standard deviation) and optical parameters (refractive index) are reported in Table 1.

According to the Mie theory, the optical thickness at the wavelength lambda is derived by the formula

$$\tau_{\lambda i}^{comp} = \tau_i^{comp} = \sum_{j=1}^{k} \int_0^{\infty} \pi r^2 Q_{extj}(m_j, r, \lambda_i) S_j n_j(r) dr, \quad (2)$$

where Q_{extj} is the extinction coefficient, m_j is the complex refractive index, and S_j is the scaling factor for the jth aerosol component. The aerosol size distributions n_j were approximated by a log-normal function. To retrieve the contribution of each aerosol component to the total AOD, the scaling factors S_j were computed with a best-fit technique by minimizing the following quantity:

$$\chi^2 = \sum_{i=1}^{N} \frac{\left(\tau_i^{meas} - \tau_i^{comp}\right)^2}{\left(\Delta\tau_i^{meas}\right)^2}, \quad (3)$$

where τ_{meas} is the measured optical depth, and τ_{comp} is the computed optical depth.

Measurement site and data set description

Instruments are hosted at the Institute of Methodologies for the Environmental Analysis (belonging to the National Research Council of Italy) located in Southern Italy (40.60° N, 15.72° E, 750 m a.s.l.).

This site is a large rural area surrounding few factories, crossed by a freeway 1 km far from the institute and characterized by a continental climate that allows measuring of mainly during the spring-summer periods, when fully sunny days, necessary for radiometric measurements, are more frequent.

The radiometric measurements data set was obtained in the period of May 2008–February 2011. Based on meteorological conditions, more than 50 days of direct solar irradiance measures have been considered in our study, corresponding to more than 1200 data analyzed. For each measurement day, spectral AODs, Ångström parameters, and aerosol size distributions were estimated each 15 min, allowing aerosol loading estimation, following the calculations described in Esposito et al. (2004).

Radiometric data were clustered according to the following procedure: days with lowest AOD values (AOD_{780} mean daily

Table 1 Physical parameters (mean radius, standard deviation) and the optical parameter refractive index describing the number size distributions of the six aerosol components

Aerosol component	r (μm)	σ	Real refr. index	Imaginary refr. index
Water-soluble (sulfate, nitrate, etc.)	0.029	2.24	1.44	−0.00265
Soot	0.018	2.0	1.75	−0.45
Sea salt (accumulation mode)	0.378	2.03	1.38	$-4.5\ 10^{-9}$
Sea salt (coarse mode)	3.17	2.03	1.38	$-4.5\ 10^{-9}$
Mineral dust	0.50	2.0	1.53	−0.0078
Biological	1.6	1.33	1.4	0.0

value ≤0.1) were classified as typical of background conditions; those with higher AOD were attributed to polluted or dust air masses, depending on the alpha values. The Hybrid Single-Particle Lagrangian Integrated Trajectory (HYPLIT4) model (Draxler and Rolph 2003). the Dust REgional Atmospheric Model (DREAM), and the Navy Aerosol Analysis and Prediction System (NAAPS) aerosol maps from the Barcelona Supercomputing Center (http://www.bsc.es/projects/earthscience/DREAM/) and the Naval Research Laboratory (http://www.nrlmry.navy.mil/aerosol/) were used as a further confirmation of the aerosol loading classification. Volcano-affected days were identified according to the VAAC atmospheric dispersion model (http://www.metoffice.gov.uk/aviation/vaac/features). To accurately describe the peculiar features characteristic of the background, polluted, dust, and volcano air masses and to avoid air masses mixing conditions, 13 days were considered among the 50-day dataset. In Table 2, for each of these aerosol classes, the measurement days and the corresponding measurement numbers are reported.

Along with the columnar aerosol measurements, simultaneous impactor sampling at the ground were conducted: the same 13 days of measurements were considered with the only difference between the two data sets that columnar data were obtained during sunlight hours, whereas in situ data were collected over a 24-h period.

In the last part of this study, one impactor sampling for each air mass, considered enough to highlight the main characteristics of deposited particles under various air masses circulation, was chosen to be examined by SEM/EDX analysis.

Radiometric data set analysis

A summary of the main aerosol parameters derived by radiometric measurements (AOD at 500 nm and at 780 nm and the alpha parameter) are reported in Table 3.

Table 2 Radiometric data set descriptions for each aerosol type

Aerosol type	Measurements days	Measurements number
Background	09 July 2008, 16 July 2008, 08 February 2011	95
Dust	27 May 2008, 08 July 2008, 16 June 10, 17 June 2010	105
Polluted	24 June 2008, 29 July 2008, 31 July 2008	75
Volcanic	21 April 2010, 29 April 2010, 13 May 2010	54

Table 3 Minimum, maximum, mean values, and corresponding standard deviations for each aerosol class

Aerosol type	Parameter	Min	Max	Mean	St. dev.
Background	AOD (500)	0.025	0.27	0.11	0.04
	AOD (780)	0.004	0.19	0.07	0.03
	Alpha	0.15	2.6	1.1	0.48
Dust	AOD (500)	0.11	0.63	0.30	0.14
	AOD (780)	0.1	0.59	0.27	0.14
	Alpha	0.03	0.8	0.39	0.18
Polluted	AOD (500)	0.14	0.33	0.21	0.05
	AOD (780)	0.03	0.19	0.09	0.04
	Alpha	1.02	3.6	1.91	0.53
Volcanic	AOD (500)	0.15	0.49	0.29	0.06
	AOD (780)	0.06	0.35	0.2	0.07
	Alpha	0.11	1.5	0.86	0.35

In particular, the minimum, maximum, mean values, and associated standard deviations for all parameters are grouped for each aerosol type and discussed.

The background conditions are characterized by both the AOD_{780} minimum and mean lowest values, typical of a poor particle loading. The alpha values range between 0.15 and 2.6 (mean value 1.1), suggesting the contribution of both small and large particles: first are related to the emissions produced by vehicular traffic and to some local anthropogenic activities, whereas second ones are likely due to the local soil particle up-lift.

In polluted conditions, that is, with air mass back trajectories crossing North/East Central Europe, the highest alpha values were recorded (maximum value 3.6, average value 1.91), whereas AOD_{780} assumes lower values than dust and volcanic conditions, as expected.

During strong Saharan dust advection, the alpha parameter ranges from 0.03 to 0.80 with an average value 0.39, typical of very large suspended aerosols. The AOD_{780} can reach values as high as 0.59. In this case, locally produced small particles do not substantially contribute to the AOD, opposite to the background conditions.

Volcanic ash data have been collected during the two main phases of the last eruption of the Eyjafjallajokull volcano (April–May 2010). The first phase (14–18 April) was characterized by tephra, ejected to over 8 km in the atmosphere, whose composition was benmoreite (Gudmundsson et al. 2012). The second explosive phase (5–17 May) was characterized by a rapid variation in the melt composition from benmoreite to trachyte, along with an increasing tephra grain size. The range of the alpha variation (0.11÷1.5) was probably affected not only by this variation in dimensions but also by a contribution to the aerosol loading of transported dust particles on May 13 and 14.

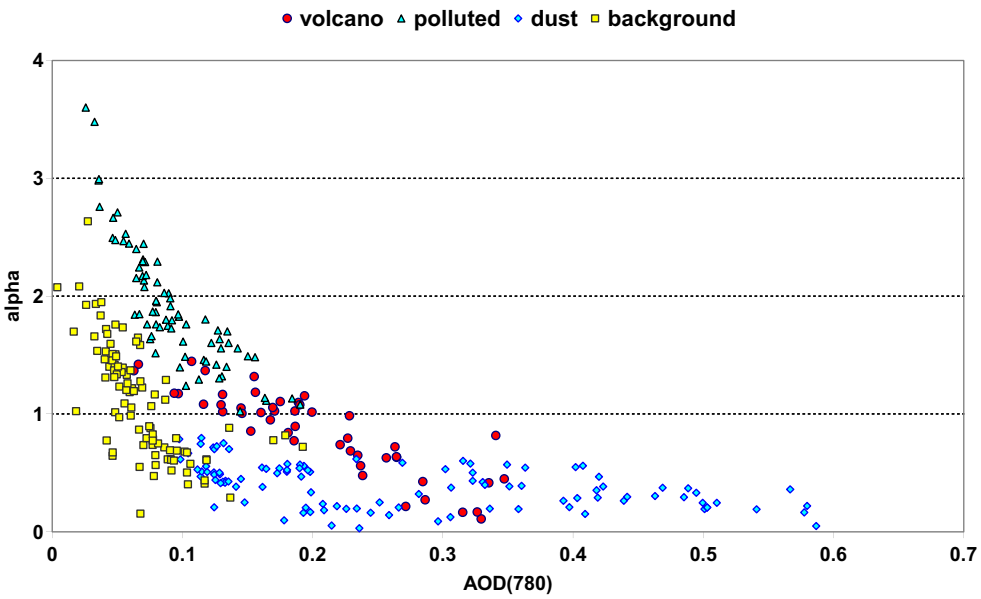

Fig. 1 Scatter-plot alpha versus AOD780. Different *shaped* and *coloured points* correspond to different aerosol families

To summarize the aerosol properties corresponding to the different air masses, scatter-plot of AOD780 and alpha parameter is reported in Fig. 1, where each particle family occupies different areas on the plot, with some overlap among different families. The background data correspond to lower AOD_{780} values (poor aerosol loading).

AOD_{780} values for polluted data are similar to background data with the corresponding points simply shifted toward higher alpha values, suggesting predominant small particles, as expected by the emissions of anthropogenic activities. In Fig. 2a, only background and polluted measurements are shown, along with the two corresponding fitting lines, which both follow a power law with the same exponent (0.59). The correlation coefficient of polluted data is higher (0.83 vs. 0.42) due to the more pronounced signature of anthropogenic particles.

Dust measurements correspond to a higher coarse particle loading even if an overlapping of the background and dust data in the regions $0.1 \leq AOD_{780} \leq 0.19$ and $0.29 \leq alpha \leq 0.67$ can be explained by considering that, in background conditions, local air circulation can favor up-lifting of soil particles in the atmosphere.

Volcano points, compared to background, cover a more extended range of AOD_{780} values ($0.06 \leq AOD_{780} \leq 0.35$), indicating a heavier aerosol content. Considering Fig. 1, polluted and volcanic data have an overlapping region defined by the following intervals: $0.06 \leq AOD_{780} \leq 0.19$ and $1.02 \leq alpha \leq 1.45$. This continuity is shown in Fig. 2b, where polluted and volcano points are reported as a whole family, which could be related to the presence of sulfate particles in both groups that are mainly produced in gas-to-particle conversion processes and are characteristic of both industrial and volcanic emissions.

Aerosol composition from columnar AODs

In Fig. 3, for each prevailing air mass (background, polluted, dust, and volcano), daily mean values of the measured AOD_{500} and model-estimated AOD_{500} for each component are reported. In general, the major components of background AODs are WS and S; only on 9 July 2008, bioparticles contribute as much as soot (approximately 24 %). On 16 July 2008, MD and bio components account respectively for 8 and 7 %, whereas on 08 February 2011, biological particles in background conditions and SScoa account for 6 and 6.7 %. This is in agreement with previous remarks about a contribution of both small and coarse fraction to the background aerosols at the site.

Polluted measurements, as expected, show a very strong contribution of WS (55–77 %), whereas soot accounts for 22–43 % of the total AOD_{500}. Remaining components give a minor contribution.

Looking at the AOD_{500} dust plot (Fig. 3c), it is interesting to note how MD is not the dominant component (from 10 to 22 %). The relevant presence of both SSacc (15–23 %) and SScoa (10–24 %) is justified by the air mass pathways, which, under Saharan particle intrusion, move from North Africa, across the Mediterranean Sea, before the arrival at the measurements site. However, the not negligible percentages of WS (11–18 %) and soot (10–27 %) seem to be surprising for trajectories coming from North Africa. In a recent study (Rodríguez et al. 2011). it has been demonstrated, by means of chemical characterization, that desert dust at the Izana Global Atmospheric Watch (GAW) Observatory in Tenerife, Canary Islands is often mixed with anthropogenic particles coming from industrial production in Northern and Eastern Algeria, Tunisia and Atlantic Morocco. In particular, they

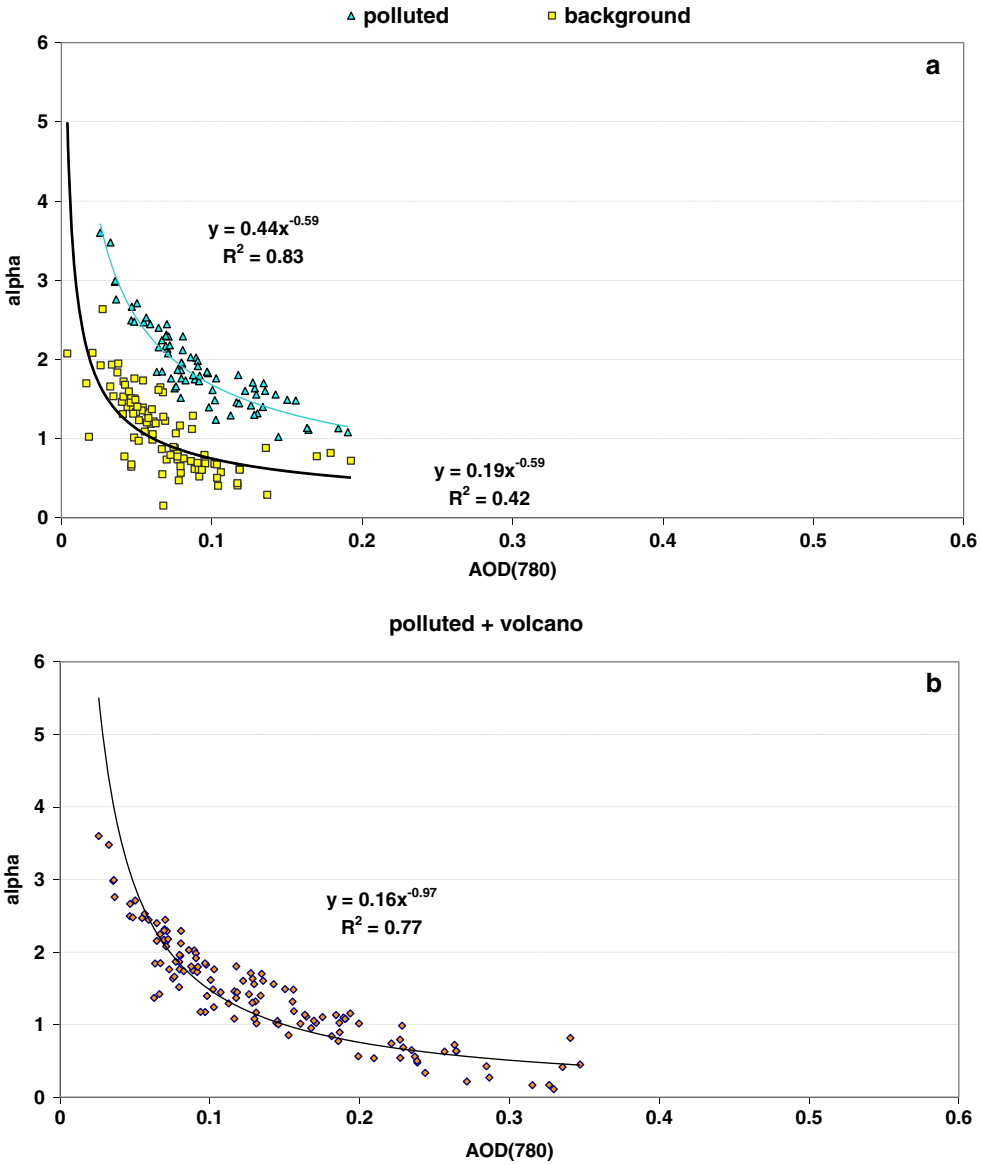

Fig. 2 Scatter-plot alpha versus AOD780. **a** For background and polluted families only. Fitting lines have the same exponent. **b** Polluted and volcano points are shown as a whole family of measurements

found crude oil refineries, phosphate-based fertilizer industry, and power plants to be responsible for nitrate, ammonium, and part of the sulfate emissions.

In Fig. 3d, volcano component clearly shows differences in the aerosol composition between 21 and 29 April 2010 and 13 May 2010, thus discriminating between the two eruption phases. In fact, the April AOD_{500} is strongly dominated by WS and soot components and, with different percentages, by MD and biological particles. During these days, the back-trajectories arose close to Iceland and moved across North Europe, thus carrying not only volcanic ash and sulfates but also industrial combustion emissions. On 13 May, back-trajectories arose again close to Iceland, but they moved across the Atlantic Ocean and Mediterranean Sea, close to North Africa, carrying higher contributions of SSacc, SScoa, and MD components.

Pie-plots in Fig. 4 reporting model-estimated mean percentages of AOD components for each air mass summarize aerosol composition variation.

Gravimetric measurements

The aerosol mass size distributions at ground level were collected by a Dekati low-pressure impactor, almost simultaneously with the radiometric data, for the 13 considered measurements days in Table 2. Plots in Fig. 5 showing mass size distributions were obtained by means of the procedure fully described in a previous work (Calvello et al. 2010). The evident features are the intense fine modes prevailing over the coarse modes for polluted days; on the contrary, the coarse modes are dominant for dust days. Comparing the volcanic

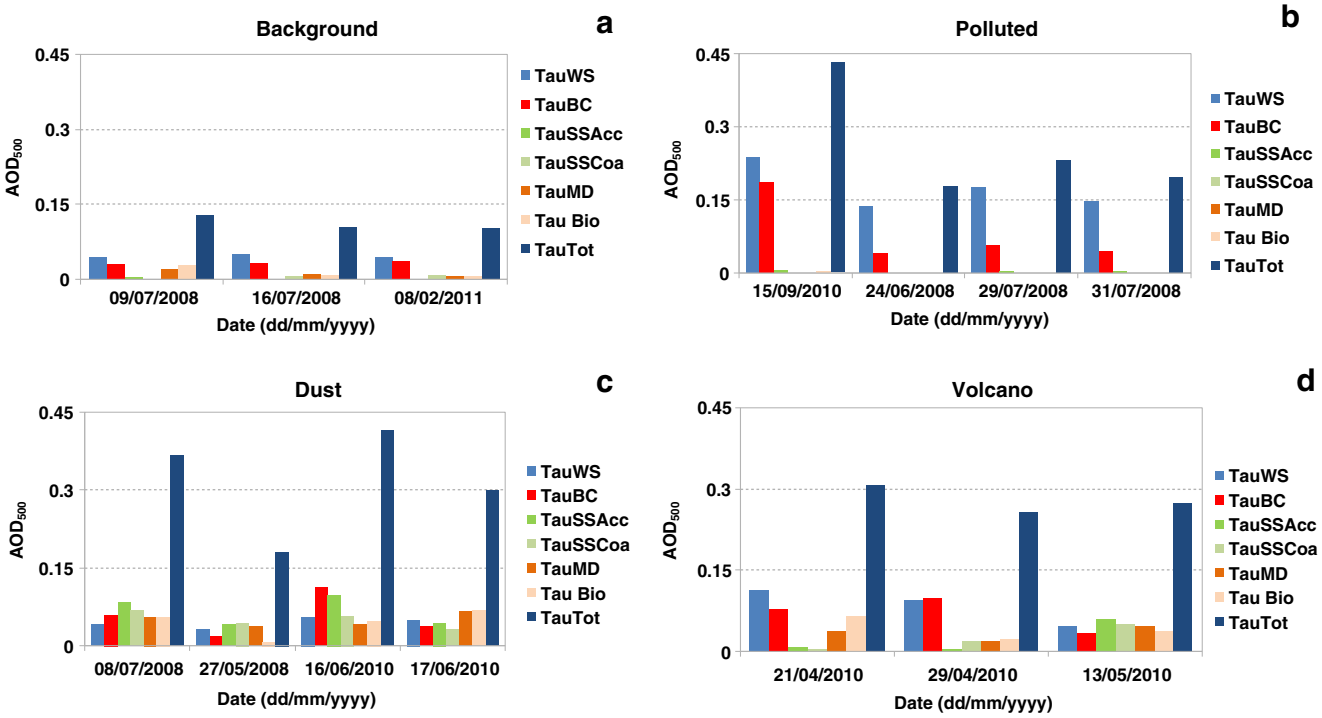

Fig. 3 Model-estimated AOD_{500} for the four air masses and for each aerosol component. *Blue bars* are the total measured AOD_{500}

size distributions on 29 April and on 13 May, an increased coarse mode is observed in the last case, in agreement with radiometric observations, related to the different eruption phases and to the advection of dust particles from North Africa on 13 May. Overall, less intense modes were obtained in the case of background conditions.

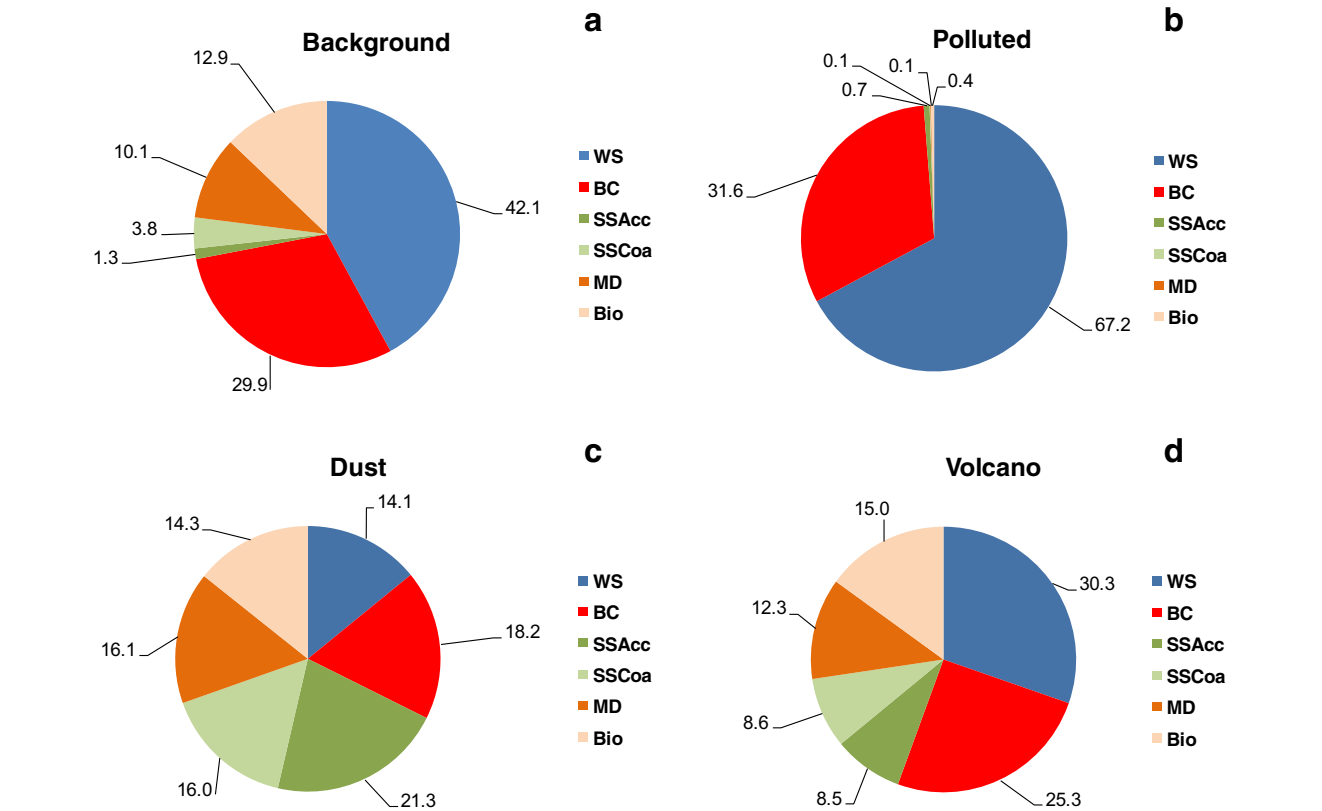

Fig. 4 Model-estimated mean percentages of AOD_{500} components for each air mass

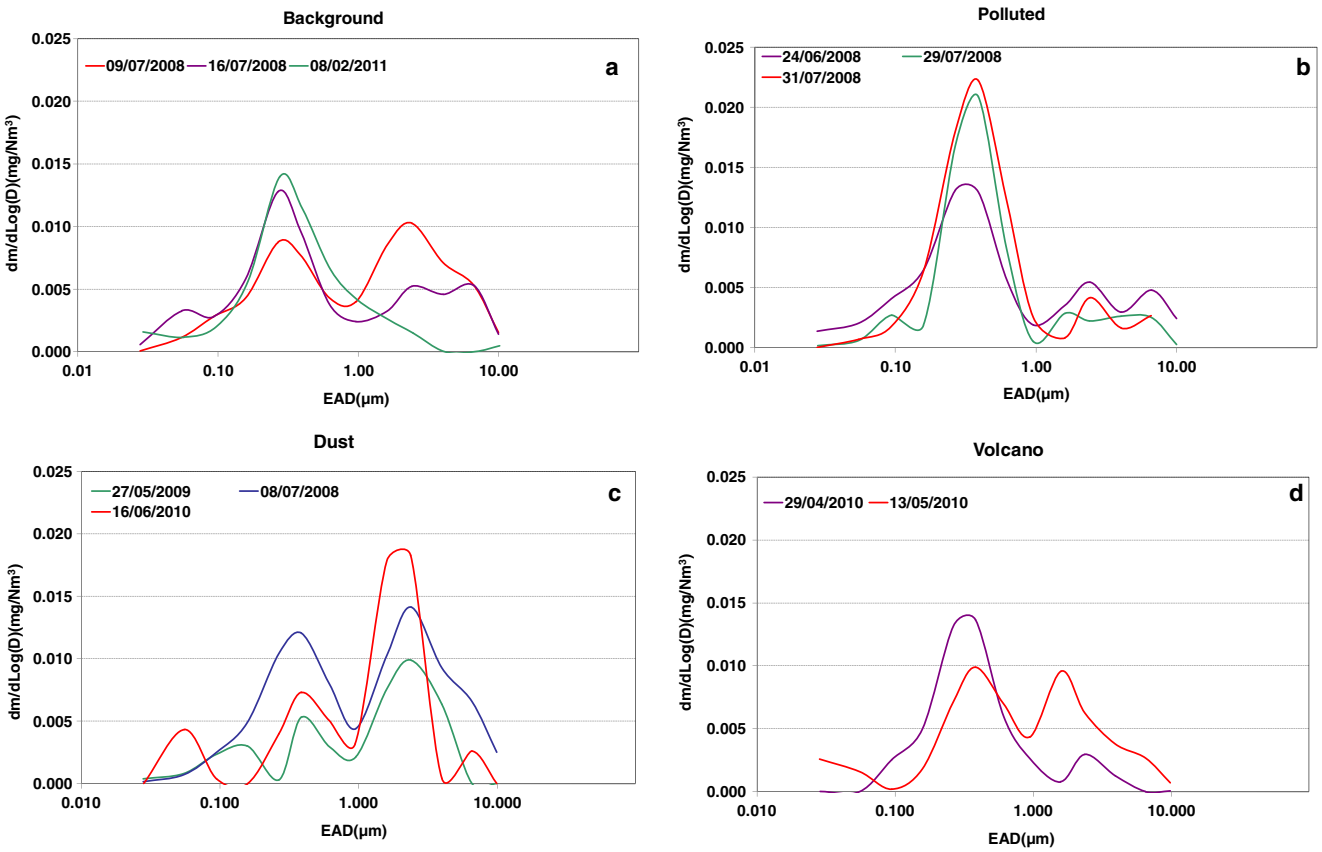

Fig. 5 Ground-based impactor mass size distributions for the four air masses

SEM/EDX analysis

Particle SEM analysis was performed on four groups of 13 DLPI polycarbonate filters, each representative of one air mass type. For each sampling, particles were grouped in fine (0.01–0.94 μm, stages 1–8) and coarse (0.94–9.77 μm, stages 9–13) fractions that have been separately observed and analyzed. As observed in a previous work (Wittmaack et al. 2002). an amorphous matter and microcrystals grown on filters prevailingly form the fine fractions of all the samplings, as it will be shown later, thus preventing quantitative analyses.

Previous observations (Mikhailov et al. 2009) help to explain the amorphous matter development. In fact, it has been shown how organic aerosols in droplet solutions, after the evaporation of the aqueous phase, are likely to aggregate in an amorphous matter and, further, how multicomponent mixtures, typical of atmospheric aerosols, can magnify these formations. As it will be explained later, SEM technique limits information on particulate because organic components cannot be detected in the fine fraction, but we cannot exclude a priori their presence. Main processes ruling the growth of microcrystals on finer stage filters, according to relative humidity and temperature variations, were deliquescence and efflorescence of inorganic salts grains, i.e., S-salts and K-salts.

Unlike the fine fraction, quantitative analysis is allowed on coarse fraction particles. This was performed for each air mass on a set of 1000 particles deposited on stages 10 and 11 (size range 1.58–3.93 μm), corresponding to the maximum of the coarse fraction mass distributions (Fig. 5a–d). Particles were divided into different classes based on the morphology and chemical composition and then gathered into ten different groups (Table 4, Fig. 6a–d). Columns in Table 4 represent groups, classes, elemental composition, morphology, and distinguishing marks, such as damage to some species under electron bombardment (Ebert et al. 2002, 2004). To compare ground-based results with columnar ones, SEM particle classes corresponding to OPAC components are reported in a further column. For each air mass, the abundance percentage of particles belonging to the different classes in stages 10 and 11 are reported. In the following, the obtained results for fine and coarse fractions corresponding to the four different air masses are discussed.

Background conditions (08 February 2011)

The amorphous matrix dominating the background fine fraction aerosol, collected in wintertime, is mainly constituted by agglomerates phases and microcrystals (Fig. 7a). The

Table 4 Groups, classes, elemental composition, morphology, distinguishing marks, and corresponding OPAC category for particles on stages 10 and 11 and for each air mass

Particle groups	Particle classes	Elemental composition	Morphology	Distinguishing marks	OPAC category	Air mass	Background		Polluted		Dust		Volcanic	
						Stage	10	11	10	11	10	11	10	11
Silicates	Illite/micas	Si-Al-K±Mg±Fe	Irregular or flake-like		MD		0	0	12	14	31	29	4	8
	Smectite	Si-Al-Ca±Mg±Fe	Irregular or flake-like		MD		19	30	8	10	16	10	0	0
	Kaolinite	Si-Al	Irregular or flake-like		MD		0	0	0	0	10	8	0	0
	Feldspar	Si-Al-Ca	Irregular		MD		0	0	2	2	0	0	0	0
	Volcanic glass	Si-Al±Ca±Mg±Na±Fe	Angular	Containing sulfur	MD		0	0	0	0	0	0	4	9
	Piroxene/amphibole	Si-Al-Ca-Mg	Irregular	Containing sulfur	MD		0	0	0	0	0	0	2	1
Silice	Quartz	Si	Irregular		MD		8	7	5	7	9	4	3	1
Carbonates	Calcite	Ca	Irregular		MD		25	18	11	15	7	16	2	9
	Dolomite	Ca-Mg	Irregular		MD		14	22	0	7	0	3	3	7
Ca-sulfates	Gypsum	Ca-S	Prismatic, columnar or acicular		MD		1	0	7	3	5	6	1	1
Sea salts	Sea Salts	Na-Cl	Cubic		SScoa		0	0	0	0	3	1	25	15
Aged sea salt	Aged sea salt	Na±Cl±S	Droplet or rhombohedral	Beam damaged	SSacc		0	0	0	0	7	14	33	39
Industrial	Fly ash	Si-Al-K-Fe	Spherical		MD		0	0	7	6	0	0	0	0
	Al oxides	Al	Spherical or irregular		MD		1	0	0	0	0	0	0	0
	Fe oxides	Fe	Spherical or irregular		MD		2	8	5	1	1	1	1	0
	Spinels	Zn±Fe	Spherical		MD		1	0	1	1	0	0	0	0
	Ca phosphates	Ca-P	Isodiammetrical		MD		0	0	1	0	0	0	1	0
	Na nitrates	Na	Deliquescent	Beam damaged	WS		2	1	7	1	0	0	0	0
	Ba sulfates	Ba-S	Isodiammetrical		MD		0	0	2	0	0	0	0	0
	Na sulfates	Na-S	Prismatic	Beam damaged	WS		0	2	0	0	0	0	0	0
	S only particles	S	Droplet		WS		0	0	1	0	0	0	0	0
Silicate mixtures	Silicate-sea-salts-carbonates-sulfates	Complex	Irregular or aggregate				5	10	5	5	3	5	17	7
Soot	Soot	No elements with Z>8	Chain or aggregate	Fractal structure	Soot		20	2	1	1	4	1	0	0
Biological	Biological	No elements with Z>8 or only K or P	Complex	Beam damaged	Bio		1	0	25	27	4	2	4	3
Total (%)							100	100	100	100	100	100	100	100

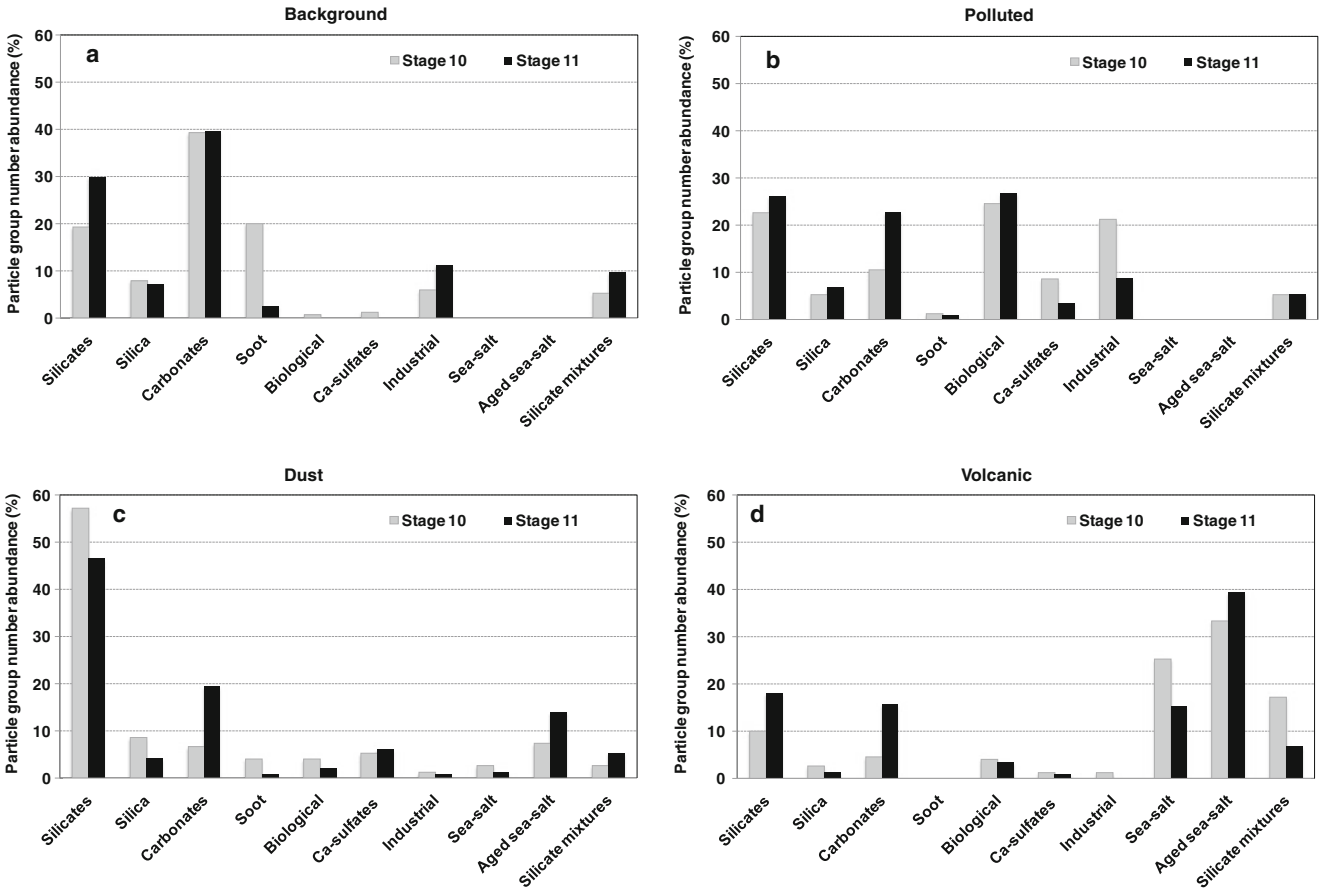

Fig. 6 Relative abundances of particle groups for stages 10 and 11 of **a** background, **b** polluted, **c** dust and **d** volcanic air masses

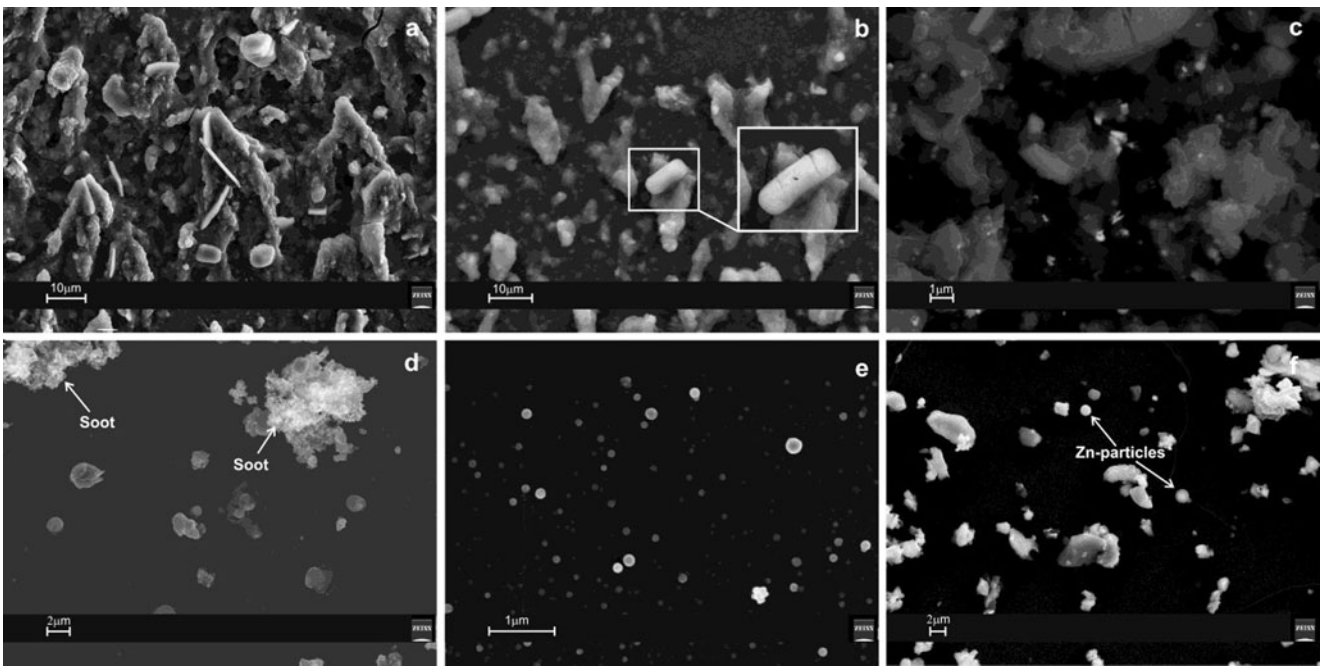

Fig. 7 SEM images of the background fine (**a**–**c**) and coarse fractions (**d**–**f**). **a** Amorphous mass and elongate crystalline phases; **b** KNO_3 crystals (*left square*) before electron bombardment and the same KNO_3 crystals (*right square*) after electron beam bombardment; **c** bright particles as metals (Fe, Pb, PbCl, and PbS); **d** soot with crystalline secondary phases inclusion; **e** Tar Balls; **f** Zn-spherical particles

chemical composition of the "soft" amorphous aerosol matter cannot be completely resolved due to the EDX inaccuracy for elements with Z≤8 (oxygen). Nevertheless, the two dominant peaks in the X-ray spectra highlight S and K, two of biomass burning tracers, as constituents of both soft matter and microcrystals. In agreement with several studies (e.g., Buseck and Pósfai 1999; Pósfai and Molnar 2000; Wittmaack et al. 2002; Ebert et al. 2002, 2004; Vester et al. 2007). SEM analysis allows attribution of the soft aerosol matter to complex secondary aerosol, such as $(NH_4)_2SO_4$, K_2SO_4, and KNO_3 (Fig. 7a). The size of crystalline particles in the soft matter was much larger than expected, as shown in Fig. 7a, b (stages 4 and 7, 0.10 μm≤EAD≤0.61 μm), where elongated crystalline phases are approximately 10 μm in size. This suggests their formation on filters due to the evaporation and recrystallization mechanisms (Dingle and Joshi 1974; Zehnder and Arnold 1989; Wittmaack et al. 2002) mainly governed by relative humidity and aerosol matter composition (Wittmaack et al. 2002).

Crystal growth matches sulfur and potassium subtraction from amorphous matter, whereas crystal damage (Fig. 7b) indicates phases characterized by weak bonds. Back-scattered electron images show the presence of metallic particles with prevailing Fe compositions and, subordinately, Pb, Pb-Cl, and Pb-S compounds (Fig. 7c).

Crustal elements (Si, Al, Fe, Mg, and Ca) are found from stages 6 and 7 (0.26–0.61 μm), whereas the corresponding chemical compounds (K and Fe aluminosilicates, Ca and Ca-Mg carbonates, and silica particles) are distinguishable in stage 8 (0.61–0.94 μm), and they are often included in soot agglomerates.

The coarse composition is characterized by high amounts of carbonate particles (approximately 40 %), silicates (20–30 %) and soot (up to 20 %), with a remarkable contribution of industrial spherical particles characterized in turn by Fe, Al, Mn, Pb, and Zn (Table 4, Fig. 6a). These elements can sometimes be found in chloride salts or in S compounds.

The presence of abundant carbonate particles is in disagreement with the local geology and soil composition (official geological cartography of Italy can be found at www.isprambiente.gov.it/Media/carg/470_POTENZA/Foglio.html), thus suggesting a local anthropogenic source. Silicate particles, mainly composed of Si and Al, with minor Ca, Fe, and/or Mg, show an irregular shape due to the mechanical production processes (e.g., windblown soil dust). Soot particles were often observed in agglomerates (Fig. 7d), sometimes with inclusion of crystalline ammonium/sodium nitrate secondary phases, suggesting RH-related deposition on soot chains, coated by aqueous and salt solutions (Lewis et al. 2009).

This fraction is also characterized by very small spherical particles (0.1–0.4 μm; Fig. 7e) without a crystal habit and resistant to electron beam impact. These characteristics correspond to tar balls (TB), particles originating from biomass burning, such as domestic wood heating, according to the sampling period (winter season) (Pósfai et al. 2004; Lewis et al. 2009; China et al. 2013). Along with TB, Zn-containing spherical particles (mean diameter 0.7 μm) and deliquescent Na-containing particles were observed (Fig. 7f). The simultaneous presence of Zn particles and Na particles suggests a common anthropogenic origin from local industrial activity (Lettino and Fiore 2013).

Polluted conditions (29 July 2008)

As in background conditions, a sulfur-rich matrix and microcrystals grown during the sampling under pollution episode characterize the fine fraction. These microcrystals vary in their form and composition, as long as they increase in size.

In particular, in stages with an EAD≤0.10 μm, prismatic crystals of ammonium nitrates are present (Fig. 8a), whereas, on stages with 0.10 μm<EAD≤0.61 μm, recrystallized phases are mainly constituted by both elongated crystals (up to 100 μm) and hexagonal tabular sulfates (ammonium-, sodium-, and potassium-sulfate) (Fig. 8b). X-ray analysis of the hexagonal tabular sulfates highlight a small amount of Zn confirmed by the back-scattered electron images. Moreover, Zn is present in this fraction as spherical single particles (Zn-oxides) or associated with Fe (spinels) (Fig. 8b). At the same time, biological particles, such as brochosomes, spores and biogenic fragments (Després et al. 2012). spherical or irregular shaped aluminosilicates, carbonates, and soot chains, appear.

The polluted coarse fraction composition (Table 4, Fig. 6b) is mostly characterized by biological particles (26 %), silicates (23–26 %), carbonates (11–22 %), and industrial particles (9–24 %) with minor amounts of sulfates, quartz, and soot. The abundance of biological particles is related to the sampling season (summer).

Silicates show two morphologies: irregular-shaped particles, typical of a terrigenous origin, and spherical particles (fly ash), produced by anthropogenic activities from heavy industrial processes (e.g., van Malderen et al. 1993; Miler and Gosar 2009) (Fig. 8c).

Terrigenous silicates show high contents of Si and Al with variable amounts of K, Ca, Fe, and/or Mg. On the contrary, the elemental composition of fly ash particles, Si, Al, K, and Fe, is rather homogenous. The fly ash concentration (7 %) indicates a relevant contribution from industrial activities.

In addition to fly ash, Al, Fe, Zn, and Fe-Zn particles constitute anthropogenic aerosols. As in the background sample, Na-containing particles, in absence of Cl, can be associated with industrial combustion processes.

Sulfates are present as barite and gypsum, which are industrial byproducts that may also be included in other matrices, such as coal, as revealed by back-scattered electrons (Fig. 8d). Simultaneous presence of barium sulfate and fly ash particles

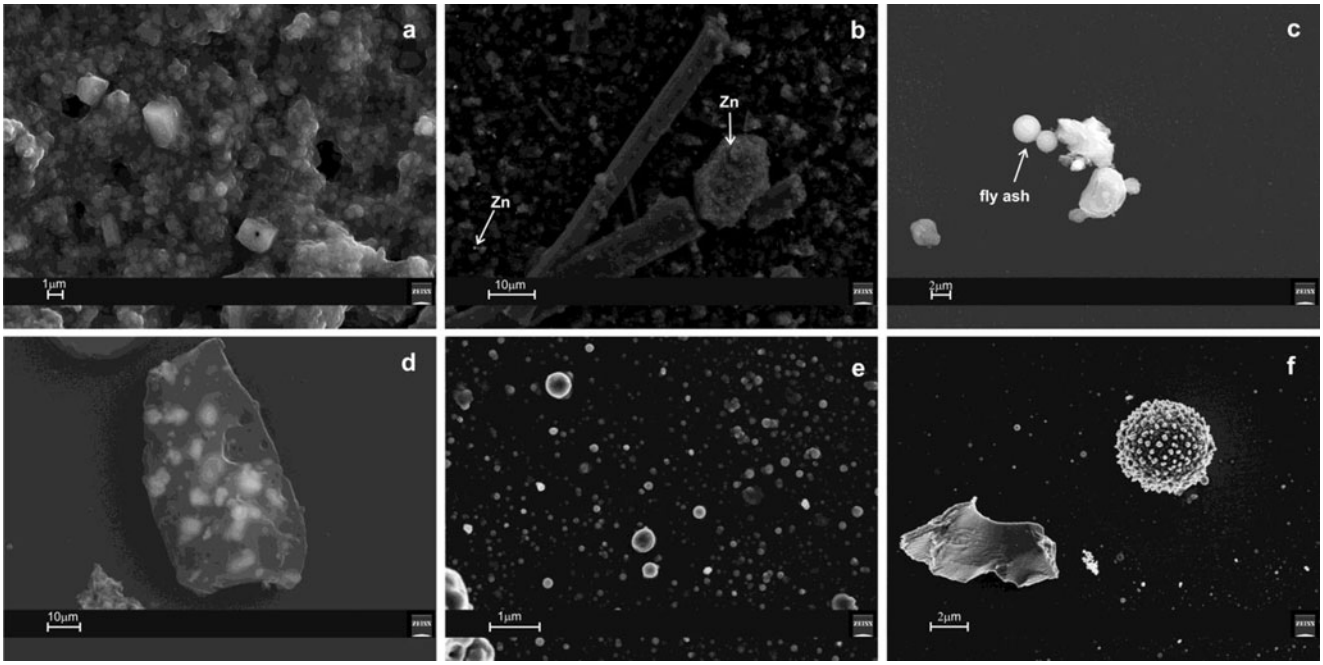

Fig. 8 SEM images of the polluted fine (**a**–**b**) and coarse fractions (**c**–**f**). **a** Crystalline growth of ammonium nitrates (prismatic crystals); **b** Zn as spherical particle and as component of sulfate crystals on stage 7; **c** silicate spheres (fly ash); **d** coal particle with inclusion of bright barite crystals; **e** Tar balls; **f** spherical biological particle and angular quartz particle

is strictly related to emissions from high-temperature industrial coal burning (Jablonska et al. 2001).

Ca-S particles mainly come from SO_2 secondary reactions of industrial emissions and from fertilizer industry (phosphates), which produces phosphogypsum (Bernabé et al. 2005). This explains the simultaneous presence of Ca-S (gypsum) and Ca-P (apatite) particles (Table 4).

As in background conditions, TB were found on polluted filters (Fig. 8e), and their detection in coarse stages could be due to the presence in the sampled air volume of larger water droplets containing them. Biological particles are detected too as shown in Fig. 8f.

Dust conditions (16 June 2010)

Unlike background and polluted air masses, particle matter collected on the impactor finer stages (EAD<0.15 μm) during Saharan dust advection is characterized by crustal elements (Si, Al) and gypsum (S-Ca), as found during the SAMUM campaign in Tinfou, Morocco (Kandler et al. 2009). These elements are enclosed in an amorphous material (Fig. 9a) with nitrates as the main component of the ultra-fine stages (EAD≤ 0.10 μm) and sulfates as the main component of the higher stages (0.1 μm<EAD≤0.6 μm).

Starting from stage 7 (EAD≈0.38 μm), aluminosilicate particles become an important constituent of the aerosol matter (Fig. 9b). They are flake-like shaped, often with K, Ca, Fe, and Mg. Sometimes these particles are captured in soot chain agglomerates (Fig. 9c).

The coarse fraction composition of dust sample (Table 4, Fig. 6c) is marked by seawater-derived particles (up to 15%), carbonates (up to 19 %), and a high content of silicate particles (up to 57%) as such as illite, smectite, and kaolinite (Fig. 9d).

Aged and fresh sea salt particles represented, respectively, by sodium nitrate (higher percentage) and NaCl (lower percentage) have been observed (Fig. 9e). Air mass pathway moving from North Africa across the Mediterranean Sea explains these types of aerosols. Fresh sea salt (NaCl containing aerosol) particles could have modified their chemical composition and morphology by losing Cl to form $NaNO_3$ (Pósfai and Molnar 2000). On the basis of SEM observations, aged sea salt crystals have rhombohedral and prismatic shapes and are beam-damaged.

Due to long-range transport, elongated gypsum crystals can be found internally mixed with clay (or with not completely transformed carbonatic particles (Fig. 9f, left side)). They are formed by heterogeneous chemical reactions involving atmospheric S compounds and carbonatic particles (Usher et al. 2002). where adsorbed SO_2 on dust particles can be oxidized to sulfate by atmospheric ozone.

Sulfur deposition on dust particles can derive from sea droplets or from anthropogenic activities, but soot aggregates externally mixed with dust particles and sulfates (Fig. 9f right side) support the second hypothesis. In observations at the GAW observatory in Izaña (Canary Islands) (Rodríguez et

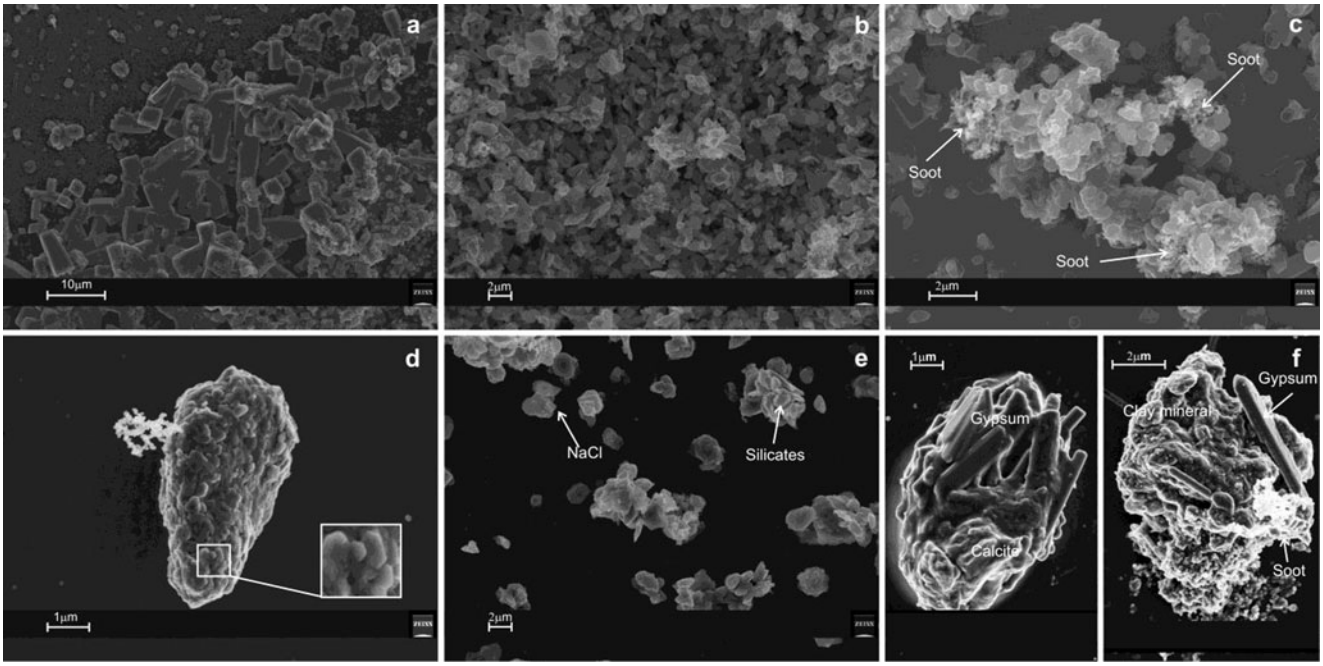

Fig. 9 SEM images of dust, fine (**a**–**c**) and coarse fractions (**d**–**f**). **a** Amorphous sub-micrometric material (*bottom-right corner*) and re-crystallized sulfate (*center*); **b** flake-like shaped aluminosilicate particles on stage 7; **c** aluminosilicate particles captured in soot agglomerate; **d** aggregate of hexagonal lamellar crystals of kaolinite; **e** silicate and sea salt particles on stage 9; **f** internally mixed state of elongated gypsum crystals with calcite (*left side*) or clay and soot particles (*right side*)

al. 2011). a clear increase of elemental carbon (soot) during dust events was found, confirming the hypothesis above. Aerosol source was not investigated, but these particles very likely derive from the same industrial process (Formenti et al. 2011).

In particular, the particle shown in Fig. 9f (right side), constituted by a soot chain externally mixed with a clay-sulfate internally mixed particle, to the authors knowledge, has never been found. In fact, observations of a large data set (101 samplings) in Cape Verde (Kandler et al. 2011) highlighted only internal mixtures of mineral dust with sulfate and soot with sulfate.

Volcano conditions (13 May 2010)

The amorphous phase of volcanic fine particles is dominated by sulfur-rich matter with some needle-shaped crystalline particles of sodium sulfates and, subordinately, of ammonium sulfates.

Sodium sulfate (mirabalite and/or thenardite) crystal sizes have been observed to grow up to 100 μm. Figure 10a shows the morphological changes of sodium sulfate crystals into double salts of $CaSO_4$ and Na_2SO_4, so called penta salt (Hill and Wills 1938). X-ray spectra of the hexagonal tabular penta-salts reveal Zn and Mg peaks (Fig. 10b). In addition to sulfates, nitrates occur as squat crystals (ammonium nitrate) or elongated thin sheets (sodium nitrate) (Fig. 10c, bottom panel).

In the coarse fraction, sulfur is not dominating anymore because a high percentage of sea salt crystals, mostly as rhombohedral crystals of sodium nitrate and some cubic-like NaCl, was observed. Their abundances can reach, in turn, 39 and 25 % of the total number of particles (Table 4, Fig. 6d).

Two mechanisms can explain the abundant NaCl crystals: the first one is the intrusion of sea water into volcano magmatic room (Allen et al. 2000). the second one is the up-lift of marine particles during the long-travel pathway of the air mass over the Atlantic Ocean and Mediterranean Sea. The highly acidic nature of volcanic plumes favored the transformation of NaCl crystals into Na_2NO_3 crystals (Mamane and Gottlieb 1992). Intermediate phases of these crystals were also found (Fig. 10d).

Among silicates, chemical composition of volcanic particles (Fig. 10e) was close to the bulk of the Eyjafjallajökull ash (trachyandesite) (Sigmundsson et al. 2010). This volcanic phase predominantly consists of angular-shaped volcanic glass and, subordinately, of particles having pyroxene/amphibole chemical compositions. They also contain sulfur, which provides a further discriminatory criterion to distinguish volcanic particles from other silicates (see Table 4).

The presence of flake-like shaped particles made of Si, Al, K, and/or Ca, as well as the well-rounded quartz particles (Fig. 10f), suggests the North African desert areas as an additional source (Coz et al. 2009). In fact, 5-day back-trajectories were crossing North Africa just before their arrival at the measurement site.

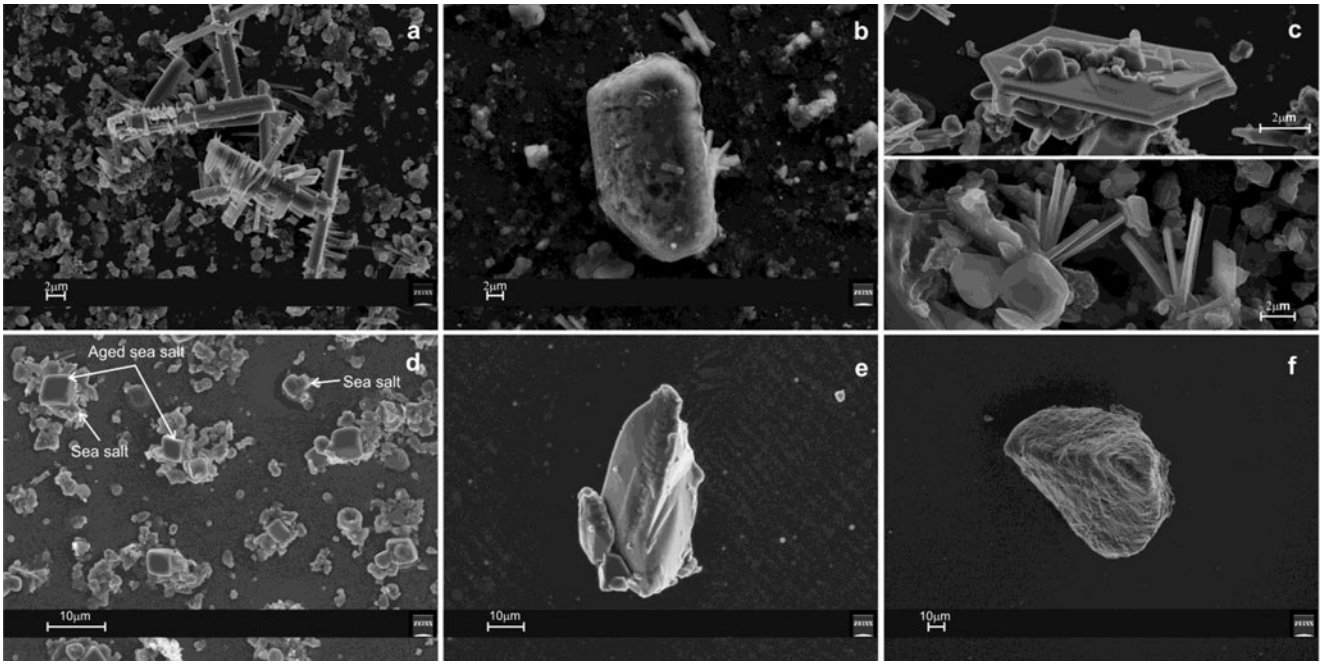

Fig. 10 SEM images of the volcanic fine (**a**–**c**) and coarse fractions (**d**–**f**). **a** Elongated sulfate crystals with orthogonal penta-salt crystals on stage 7; **b** hexagonal tabular sulfate with Zn and Mg; **c** lamellar hexagonal Na-K sulfate crystal (*top panel*) and elongated thin sheet sodium nitrate crystals (*bottom panel*); **d** sea salts and aged sea salts particles on stage 9; **e** volcanic glass particle; **f** rounded quartz particle

Discussion and conclusions

The absence of local strong sources at the semirural measurement site represents a useful condition to study background aerosol loading, to compare aerosol-mixing effects under different air masses circulation, both at the ground and over the column, and to study morphological and compositional modifications of aerosol properties due to the long-range transport. According to the radiometric measurements clustering procedure, 13 days were considered in this study, and 4 gravimetric samplings were considered representative for SEM analysis of the four different aerosol loadings.

Despite the air mass pathways, similarities were found between columnar and ground observations and among ground-based collected particles.

In background conditions, fine and coarse particles can give comparable contributions over the column, as inferred from the wide range of the alpha parameter variation (0.15÷2.6), and from the ground-based mass size distributions showing similar amplitudes of fine and coarse modes. Small industrial activities and a freeway running 1 km far from the site heavily contribute to the aerosol composition: on average, anthropogenic particles (WS and soot) account for 72 % of the total AOD (Fig. 4a). This is in good agreement with SEM/EDX analysis observations of industrial, non-crustal carbonatic particles and soot accounting for about 60 % of the coarse fraction, as in Fig. 6a.

Under polluted air masses, the fine fraction prevails on both radiometric and gravimetric measurements with WS and soot dominating (99 %) the columnar composition (Fig. 4b).

Sulfur is present in recrystallized phases constituted by both elongated crystals (up to 100 μm) and hexagonal tabular sulfates (ammonium-, sodium-, and potassium-sulfate) on which, sometimes, a small amount of Zn is present. Zn was also found as individual spherical particles or associated with Fe. Coarse fraction composition, as reported in Fig. 6b, reveals 26 % of biological particles and 39 % of anthropogenic particles among which gypsum and apatite (fertilizer manufacturing), fly ash and S-Ba in coal particles (high temperature combustion processes), and metal-rich and deliquescent sodium nitrate particles are a clear signature of anthropogenic activities.

Under Saharan dust advection, large particles significantly contribute to both columnar and in situ measurements (AOD_{780} increase and alpha reduction over the column, a dominating coarse mode over the column and at the ground). MD characterizes columnar aerosol composition, but it contributes likewise SS, WS, soot and bio, clearly indicating the influence of natural and anthropogenic sources on the aerosol composition (Fig. 4c). At the ground, crustal elements (gypsum and aluminosilicate often with K, Ca, Fe, and Mg) are detected by SEM-EDX analysis since the fine fraction. Soot aggregates mixed with dust particles and sulfates in the coarse fraction indicate the interaction between primary particles from crude oil refineries and power plants located along the

North African coast and Saharan dust, whereas heterogeneous chemical reactions involving S-compounds on carbonatic particles produce elongated gypsum crystals internally mixed with clay.

In addition, sea salt aerosols are the main components of the coarse fraction, accounting with dust particles for 71 % of total particles (Fig. 6c). It is worth noting, once again, common features (sea salt particles, soot and mineral dust etc.) in the results from columnar and ground-based data analysis.

Depending on the eruptive phase (April or May 2010), the volcanic plume from the Eyjafjallajokull eruption produced different effects on the aerosol properties. In fact, WS and soot dominated in April, whereas SS and MD increased their contribution in May also due to a contemporary advection of Saharan dust (Fig. 4d). Corresponding gravimetric size distributions were bimodal for both the April and May measurements, but, in May, the coarse and fine modes are equally intense (Fig. 5d). From SEM analysis of the May sampling, volcanic, mineral particles and sea salts dominate the coarse fraction (Fig. 6d). A clear signature of volcanic eruption is provided by trachyandesite particles, the same as the Eyjafjallajökull bulk composition, whereas flake-like particles made of Si, Al, K, and/or Ca are indicative of a Saharan desert contribution. The fine fraction shows a sulfur-rich matter with crystal particles of sodium sulfate and sodium nitrate. In larger stages of the fine fraction (stage 8), sodium sulfate crystals modify their composition becoming $CaSO_4$, $MgSO_4$, K_2SO_4.

In the effort to make a uniform classification of columnar and ground-based data, single coarse particles observed by SEM have been classified according to the OPAC categories as in Table 4. Corresponding percentages are reported in Fig. 11a–d, where discrepancies with columnar data (Fig. 4a–d) are evident, since MD represents the main component for all air masses at the ground. This can be explained by different reasons: first is that opposite to columnar optical properties, SEM quantitative analysis is referred to the coarse fraction only. As an example, nitrates belonging to the WS columnar component are absent in the ground-based coarse fraction. Second, MD particles over the column are related to natural mineral transported aerosol, whereas SEM-derived MD category includes both natural (silicates, silica, Ca-sulfates) and anthropogenic insoluble particles (fly ash, carbonates, Ca and Ba-sulfates, metal-oxides, etc.).

Notwithstanding these differences, remarkable common features, both at the ground and over the column, were highlighted. Among these, sulfates, which are common to

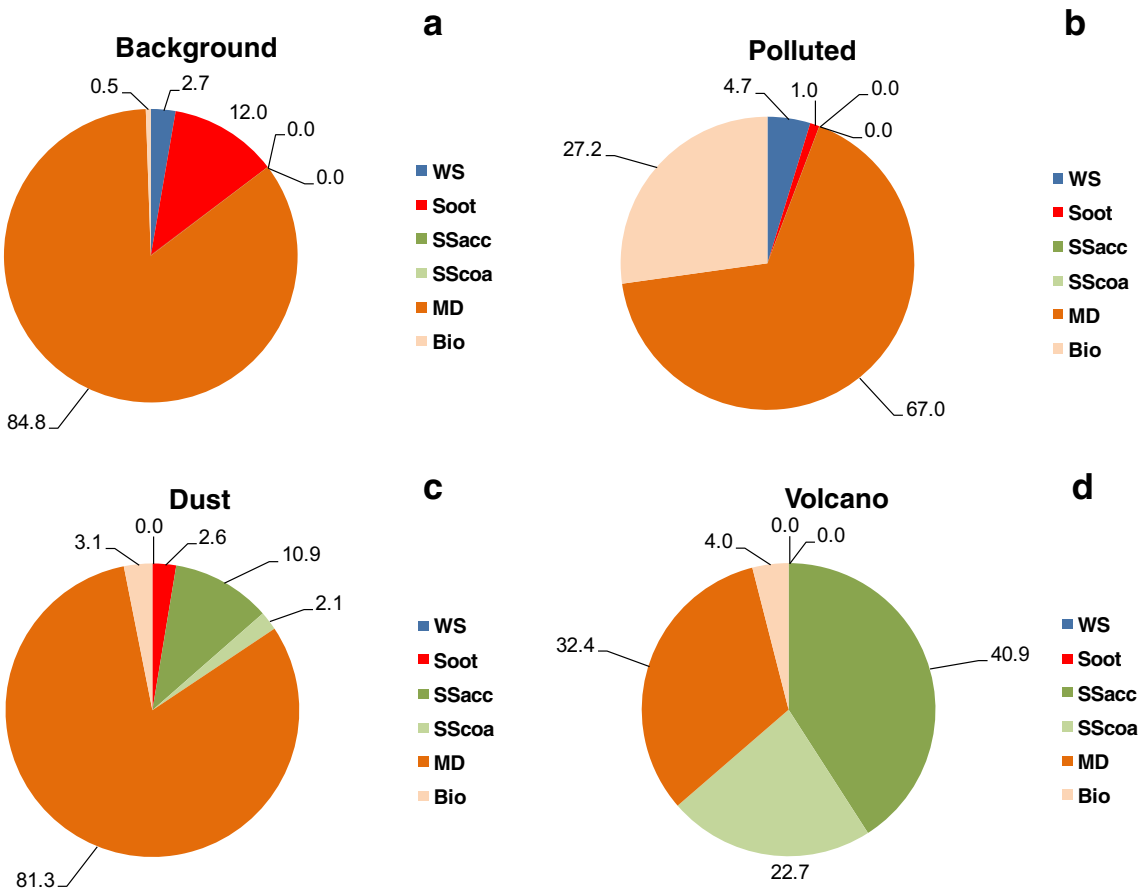

Fig. 11 Pie-plot of coarse aerosol grouped according to OPAC model components observed with SEM for **a** background, **b** polluted, **c** dust, **d** volcanic air masses

the different air masses, are found to be one of the major components of the amorphous matrix produced by the evaporation of solutions of both organic and inorganic aerosols. Besides, in the measurement area, sulfates are one of the principal players involved in heterogeneous chemical reactions, producing internally mixed secondary aerosol and modifying optical properties and size distributions of primary particles (i.e., soot or dust mineral).

In general, radiative transfer models could not disregard long-range transport processes, such as secondary phase formation and particle external mixing, metal-bearing clay minerals, metal particles, and sulfates internally mixed. Consequently, this study can represent a step ahead to satisfy the modeler's requests for a more detailed description of the aerosol composition, both at the ground and over the atmospheric column.

Finally, these findings should motivate scientists to study aerosol mixing states, extending them to sites with different local sources and air mass circulations to improve, i.e., radiative models results.

Acknowledgments Authors would like to thank the three anonymous referees for their useful comments and suggestions which helped improve the paper quality.

This study was partially financially supported by the Associazione Italiana per lo Studio delle Argille - onlus.

Authors are thankful to the NOAA Air Resources Laboratory (ARL) for HYSPLIT model and READY website (http://www.arl.noaa.gov/ready.php) allowing air mass calculation and to the NRL/Monterey Aerosol Page for NAAPS maps used in this study. Authors would like to acknowledge the Barcelona Super-Computing Centre for DREAM dust maps provision.

References

Allen AG, Baxter PJ, Ottley CJ (2000) Gas and particle emissions from Soufrière Hills volcano, Montserrat, West Indies: characterization and health hazard assessment. Bull Volcanol 62:8–19

Amato U, Esposito F, Serio C, Pavese G, Romano F (1995) Inverting high spectral resolution aerosol optical depth to determine the size distribution of atmospheric aerosol. Aerosol Sci Technol 23:591–602

Bauer SE, Ault A, Prather KA (2013) Evaluation of aerosol mixing state classes in the GISS model E-MATRIX climate model using single-particle mass spectrometry measurements. J Geophys Res 118: 9834–9844

Bernabé JM, Carretero MI, Galán E (2005) Mineralogy and origin of atmospheric particles in the industrial area of Huelva (SW Spain). Atmos Environ 39:6777–6789

Bovchaliuk A, Milinevsky G, Danylevsky V, Goloub P, Dubovik O, Holdak A, Ducos F, Sosonkin M (2013) Variability of aerosol properties over Eastern Europe observed from ground and satellites in the period from 2003 to 2011. Atmos Chem Phys 13:6587–6602

Buseck PR, Pósfai M (1999) Airborne minerals and related aerosol particles: effects on climate and the environment. Proc Natl Acad Sci 96(7):3372–3379

Calvello M, Esposito F, Pavese G, Serio C (2010) Physical and optical properties of atmospheric aerosol by in situ and radiometric measurements. Atmos Chem Phys 10:2195–2208

Cheng T, Wu Y, Gu X, Chen H (2015) Effects of mixing states on the multiple scattering properties of soot aerosols. Opt Express 23:8. doi:10.1364/OE.23.010808

China S, Mazzoleni C, Gorkowski K, Aiken AC, Dubey MK (2013) Morphology and mixing state of individual freshly emitted wildfire carbonaceous particles. Nat Commun. doi:10.1038/ncomms3122

Coz E, Gómez-Moreno FJ, Pujadas M, Casuccio GS, Lersch TL, Artinano B (2009) Individual particle characteristics of North African dust under different long-range transport scenarios. Atmos Environ 43:1850–1863

de Villiers RA, Ancellet G, Pelon J, Quennehen B, Schwarzenboeck A, Gayet JF, Law KS (2010) Airborne measurements of aerosol optical properties related to early spring transport of mid-latitude sources into the Arctic. Atmos Chem Phys 10:5011–5030

Després RV, Huffman JA, Burrows SM, Hoose C, Safatov AS, Buryak G, Frölich-Nowoisky J, Elbert W, Andreae MO, Pöschl U, Jaenicke R (2012) Primary biological aerosol particles in the atmosphere: a review. Tellus B 64:15598. doi:10.3402/tellusb.v64i0.15598

Dingle AN, Joshi BM (1974) Ammonium sulphate crystallization in Andersen Cascade impactor samples. Atmos Environ 8:1119–1130

Draxler RR, Rolph GD (2003) HYSPLIT (Hybrid Single-Particle Lagrangian Integrated Trajectory) model, http://www.arl.noaa.gov/ready/hysplit4.html, NOAA Air Resour. Lab., Silver Spring, MD

Ebert M, Weinbruch S, Hoffmann P, Ortner HM (2000) Chemical characterization of North Sea aerosol particles. J Aerosol Sci 31:613–632

Ebert M, Weinbruch S, Rausch A, Gorzawski G, Hoffmann P, Wex H, Helas G (2002) The complex refractive index of aerosols during LACE 98 as derived from the analysis of individual particles. J Geophys Res 107(D21):8121

Ebert M, Weinbruch S, Hoffmann P, Ortner HM (2004) The chemical composition and complex refractive index of rural and urban influenced aerosols determined by individual particle analysis. Atmos Environ 38:6531–6545

Eguchi K, Uno I, Yumimoto K, Takemura T, Shimizu A, Sugimoto N, Liu Z (2009) Trans-pacific dust transport: integrated analysis of NASA/CALIPSO and a global aerosol transport model. Atmos Chem Phys 9:3137–3145

Esposito F, Leone L, Pavese G, Restieri R, Serio C (2004) Seasonal variation of aerosols properties in South Italy: a study on aerosol optical depths Ångström turbidity parameters and aerosol size distributions. Atmos Environ 38(11):1605–1614

Formenti P, Schűtz L, Balkanski Y, Desboeufs K, Ebert M, Kandler K, Petzold A, Scheuvens D, Weinbruch S, Zhang D (2011) Recent progress in understanding physical and chemical properties of African and Asian mineral dust. Atmos Chem Phys 11:8231–8256

Gudmundsson MT, Thordarson T, Höskuldsson A, Larsen G, Björnsson H, Prata FJ, Oddsson B, Magnusson E, Högnadottir T, Petersen GN, Hayward CL, Stevenson JA, Jonsdottir I (2012) Ash generation and distribution from the April-May 2010 eruption of Eyjafjallajokull, Iceland. Nat Sci Rep 2:572. doi:10.1038/srep00572

Hess M, Koepke P, Schult I (1998) Optical properties of aerosols and clouds: the software package OPAC. Bull Am Meteorol Soc 79: 831–844

Hill AE, Wills JH (1938) Ternary systems. XXIV. Calcium sulfate, sodium sulfate and water. J Am Chem Soc 60:1647–1655

Huffman JA, Treutlein B, Poschl U (2010) Fluorescent biological aerosol particle concentrations and size distributions measured with an ultraviolet aerodynamic particle sizer (UV-APS) in Central Europe. Atmos Chem Phys 10:3215–3233

IPCC Intergovernmental Panel on Climate Change, Climate Change (2007) The physical science basis: contribution of working group I to the fourth assessment report of the intergovernmental panel on climate change. Cambridge University Press, Cambridge

Jablonska M, Rietmeijer FJM, Janeczek J (2001) Fine-grained barite in coal fly ash from the upper Silesian Industrial Region. Environ Geol 40:941–948

Kandler K, Schütz L, Deutscher C, Ebert M, Hofmann H, Jäckel S, Jaenicke R, Knippertz P, Lieke K, Massling A, Petzold A, Schladitz A, Weinzierl B, Wiedensohler A, Zorn S, Weinbruch S (2009) Size distribution, mass concentration, chemical and mineralogical composition and derived optical parameters of the boundary layer aerosol at Tinfou, Morocco, during SAMUM 2006. Tellus 61B:32–50

Kandler K, Lieke K, Benker N, Emmel C, Kupper M, Muller-Ebert D, Ebert M, Scheuvens D, Schladitz A, Schütz L, Weinbruch S (2011) Electron microscopy of particles collected at Praia, Cape Verde, during the Saharan mineral dust experiment: particle chemistry, shape, mixing state and complex refractive index. Tellus 63B:475–496

Latha R, Murthy BS, Kumar M, Jyotsna S, Lipi K, Pandithurai G, Mahanti NC (2014) Aerosol optical properties and composition over a table top complex mining area in a monsoon trough region. Aerosol Air Qual Res 14:806–817

Lettino A, Fiore S (2013) Provenance of inorganic aerosol using single-particle analysis: a case study. Sci Total Environ 463–464:404–413

Lettino A, Caggiano R, Fiore S, Macchiato M, Sabia S, Trippetta S (2012) Eyjafjallajökull volcanic ash in southern Italy. Atmos Environ 48:97–103

Lewis KA, Arnott WP, Moosmuller H, Chakrabarty RK, Carrico CM, Kreidenweis SM, Day DE, Malm WC, Laskin A, Jimenez JL, Ulbrich IM, Huffman JA, Onasch TB, Trimborn A, Liu L, Mishchenko MI (2009) Reduction in biomass burning aerosol light absorption upon humidification: roles of inorganically- induced hygroscopicity, particle collapse, and photoacoustic heat and mass transfer. Atmos Chem Phys 9:8949–8966

Li W, Shao LY, Shen R, Wang Z, Yang S, Tang U (2010) Size, composition and mixing state of individual aerosol particles in South China coastal city. J Environ Sci 22:561–569

Mamane Y, Gottlieb J (1992) Nitrate formation on sea-salt and mineral particles—a single particle approach. Atmos Environ 26(9): 1763–1769

Matthias-Maser S, Jaenicke R (1995) The size distribution of primary biological aerosol particles with radii >0.2 μm in an urban/rural influenced region. Atmos Res 39:279–286

Mikhailov E, Vlasenko S, Martin ST, Koop T, Pöschl U (2009) Amorphous and crystalline aerosol particles interacting with water vapor: conceptual framework and experimental evidence for restructuring, phase transitions and kinetic limitations. Atmos Chem Phys 9:9491–9522

Miler M, Gosar M (2009) Characterisation of solid airborne particles in urban snow deposits from Ljubljana by means of SEM/EDS. RMZ-Mater Geoenviron 56(3):266–282

Papayannis A, Balis D, Amiridis V, Chourdakis G, Tsaknakis G, Zerefos C, Castanho ADA, Nickovic S, Kazadzis S, Grabowski J (2005) Measurements of Saharan dust aerosols over the Eastern Mediterranean using elastic backscatter-Raman lidar, spectrophotometric and satellite observations in the frame of the EARLINET project. Atmos Chem Phys 5:2065–2079

Pavese G, De Tomasi F, Calvello M, Esposito F, Perrone MR (2009) Detection of Sahara dust intrusions during mixed advection patterns over south-east Italy: a case study. Atmos Res. doi:10.1016/j.atmosres.2009.02.003

Pavese G, Calvello M, Esposito F, Leone L, Restieri R (2012) Effects of Saharan dust advection on atmospheric aerosol properties in the West-Mediterranean area. Adv Meteorol. doi:10.1155/2012/730579

Pederzoli A, Mircea M, Finardi S, di Sarra A, Zanini G (2010) Quantification of Saharan dust contribution to PM10 concentrations over Italy during 2003–2005. Atmos Environ 44:4181–4190

Perrone MR, Romano S, Orza JAG (2015) Columnar and ground-level aerosol optical properties: sensitivity to the transboundary pollution, daily and weekly patterns, and relationships. Environ Sci Pollut Res. doi:10.1007/s11356-015-4850-7

Pósfai M, Molnar A (2000) Aerosol particles in the troposphere: a mineralogical introduction. EMU Notes Miner 2:197–252

Pósfai M, Gelencser A, Simonics R, Arato K, Li J, Hobbs PV, Buseck PR (2004) Atmospheric tar balls: particles from biomass and biofuel burning. J Geophys Res 109:D06213. doi:10.1029/2003JD004169

Rodríguez S, Alastuey A, Alonso-Pérez S, Querol X, Cuevas E, Abreu-Afonso J, Viana M, Pérez N, Pandolfi M, de la Rosa J (2011) Transport of desert dust mixed with North 15 African industrial pollutants in the subtropical Saharan Air Layer. Atmos Chem Phys 11:6663–6685. doi:10.5194/acp-11-6663

Satheesh SK, Srinivasan J (2005) A method to estimate aerosol radiative forcing from spectral optical depths. J Atmos Sci 63:1082–1092

Sciare J, Oikonomou K, Favez O, Liakakou E, Markaki Z, Cachier H, Mihalopoulos N (2008) Long-term measurements of carbonaceous aerosols in the Eastern Mediterranean: evidence of long-range transport of biomass burning. Atmos Chem Phys 8:5551–5563

Shi Z, Shao L, Jones TP, Whittaker AG, Lu S, Bérubé KA, He T, Richards RJ (2003) Characterization of airborne individual particles collected in an urban area, a satellite city and a clean air site in Beijing, 2001. Atmos Environ 37:4097–4108. doi:10.1016/S1352-2310(03)00531-4

Sigmundsson F, Hreinsdóttir S, Hooper A, Árnadóttir T, Pedersen R, Roberts MJ, Óskarsson N, Auriac A, Decriem J, Einarsson P, Geirsson H, Hensch M, Ófeigsson BG, Sturkell E, Sveinbjörnsson H, Feigl KL (2010) Intrusion triggering of the 2010 Eyjafjallajökull eruption. Nature 468:426–430

Sinha PR, Manchanda RK, Kaskaoutis DG, Kumar YB, Sreenivasan S (2013) Seasonal variation of surface and vertical profile of aerosol properties over a tropical urban station Hyderabad, India. J Geophys Res 118:749–768. doi:10.1029/2012JD018039

Tiwari S, Pipal AS, Hopke PK, Bisht DS, Srivastava AK, Tiwari S, Saxena PN, Khan AH, Pervez S (2015) Study of the carbonaceous aerosol and morphological analysis of fine particles along with their mixing state in Delhi, India: a case study. Environ Sci Pollut Res. doi:10.1007/s11356-015-4272-6

Usher CR, Al-Hosney H, Carlos-Cuellar S, Grassian VH (2002) A laboratory study of the heterogeneous uptake and oxidation of sulfur dioxide on mineral dust particles. J Geophys Res 107(D23):4713. doi:10.1029/2002JD002051

van Beelen AJ, Roelofs GJH, Hasekamp OP, Henzing JS, Röckmann T (2014) Estimation of aerosol water and chemical composition from AERONET Sun–sky radiometer measurements at Cabauw, the Netherlands. Atmos Chem Phys 14:5969–5987

Van Malderen H, De Bock LA, Injuk J, Xhoffer C, Van Grieken R (1993) North Sea aerosol characterization by single particle analysis techniques. Prog Belg Oceanogr Res Brussels 21–22:119–135

Vedal S, Hannigan MP, Dutton SJ, Miller SL, Milford JB, Rabinovitch N, Kim NS-Y, Sheppard L (2009) The Denver Aerosol Sources and Health (DASH) study: overview and early findings. Atmos Environ 43:1666–1673

Vester BP, Ebert M, Barnert EB, Schneider J, Kandler K, Schutz L, Weinbruch S (2007) Composition and mixing state of the urban background aerosol in the Rhein-Main area (Germany). Atmos Environ 41(29):6102–6115

Wittmaack K, Menzel N, Wehnes H, Heinzmann U (2002) Phase separation and regrowth of aerosol matter collected after size fractionation in an impactor. Atmos Environ 36:5877–5886

Zehnder K, Arnold A (1989) Crystal growth in salt efflorescence. J Cryst Growth 97:513–521